

Hydrodynamic interactions in ordering process of two-dimensional quenched block copolymers

Y. Yokojima and Y. Shiwa

Division of Materials Science, Kyoto Institute of Technology, Matsugasaki, Sakyo-ku, Kyoto 606-8585, Japan

(Received 23 January 2002; published 15 May 2002)

The hydrodynamic coarsening of microphase separation in two-dimensional diblock copolymers is studied using numerical simulations. Results for symmetric and asymmetric block copolymers are compared. In contrast to the formation of the hexagonal phase where hydrodynamic flow appears not to be effective in enhancing domain coarsening, the late-time evolution of the lamellar phase proceeds faster, thus leading to a different power-law scaling with the addition of coupling of the velocity field to the order parameter.

DOI: 10.1103/PhysRevE.65.056308

PACS number(s): 47.20.-k, 61.41.+e, 47.54.+r, 64.60.Cn

I. INTRODUCTION

When a system is transferred from a homogeneous phase to an ordered phase where the initial state is thermodynamically unstable, a network of small domains of ordered phase develops spontaneously and the length scale associated with these domains grows with time. In systems such as a binary mixture, this domain coarsening proceeds to form macroscopic domains (hence termed macrophase separation). In this paper we focus on block copolymers, a system in which coarsening cannot proceed to a macroscopic scale.

A characteristic feature of the block copolymers is the connectivity between chemically distinct building blocks. Due to this severe constraint a phase separation, which occurs at low enough temperatures, can segregate at best to the mesoscopic length scale. This so-called microphase separation produces spatially periodic patterns. The existence of the spatial period $2\pi/q_0$ of the ordered structure renders the study of microphase separation kinetics quite intriguing in comparison with the case of macrophase separation for which $q_0=0$.

It is now generally accepted [1] that, during the late stages of macrophase separation, there is dynamical self-similarity, where morphologies at different times can be related by a single characteristic length $L(t)$. In general, this length grows as a power law in time, $L(t) \sim t^n$, where n is called the growth exponent. A large number of systems can then be grouped into a small number of universality classes characterized by a common exponent n depending only on certain relevant system characteristics and not on the details of the particular system. One of the relevant features that influence the growth law is the presence of the coupling between the order parameter and the hydrodynamic velocity fields. When the hydrodynamic interactions are operative it is well known that the coarsening proceeds much faster, although the exact value of the growth exponent remains incompletely understood [2].

In the microphase separation, however, the situation is far from clear. No successful theoretical formulation is yet available for the domain coarsening in the absence of hydrodynamic fields. Exponents n ranging from 1/5 to 1/2 have been reported (mostly from numerical simulations) [3,4]. There is even a suggestion of breakdown of the universality [5].

Therefore it is no surprise to find that the problem of hydrodynamic coarsening in block copolymers has been little

exploited using numerical studies. However, the dynamical scale invariance of coarsening is scarcely addressed, either because the simulations are performed on a rather small lattice (hence a system freezes at long times and the pathway toward this state is too short to exhibit a possible asymptotic scaling behavior) [6,7] or because the coarsening has not been followed through the average domain size (which is most commonly measured in macrophase separation studies) [8,9]. Consequently, the role of velocity fields remains a source of controversy.

In what follows, we undertake a detailed numerical analysis of the growth law of domain evolution in the coarsening of microphase separating block copolymers with hydrodynamic flow. In Sec. II we introduce a time-dependent Ginzburg-Landau-type model for the ordering dynamics of lamellar patterns, which incorporates the hydrodynamic coupling of the order parameter field. Our simulation is facilitated by the use of computationally efficient cell-dynamical-system (CDS) method, which has quite successfully elaborated the nature of macrophase separation [10]. In Sec. III we present numerical results for the correlation function of the order parameter (scattering function) and the orientational correlation function of the lamellar domains. With these correlation functions, quantitative study of the growth exponent is provided. In order to address the important question that whether hydrodynamic interactions are equally important for both symmetric copolymers and asymmetric copolymers, we study in Sec. IV the kinetics of microphase separation into the hexagonal phase. Section V concludes this paper with a summary and discussion.

II. DYNAMICAL MODEL

A. TDGL equations for lamellar formation

In this section we consider A - B diblock copolymers with equal-length subchains, in which an ordered layered phase with alternating A and B rich domains (lamellae) is formed. We investigate formation of the lamellar state in two dimensions with rotational invariance in the plane. The model to describe its dynamics is the following time-dependent Ginzburg-Landau (TDGL) equation for the order parameter ψ :

$$\frac{\partial \psi}{\partial t} = M \nabla^2 \frac{\delta H\{\psi\}}{\delta \psi} - (\mathbf{v} \cdot \nabla) \psi. \quad (1)$$

The $\psi(\mathbf{r}, t)$ is the scalar order parameter at a space-time point (\mathbf{r}, t) , chosen to be the local monomer concentration difference of A and B species. The free energy functional $H\{\psi\}$ is given by

$$\beta H\{\psi\} = H_s\{\psi\} + H_l\{\psi\}, \quad (2)$$

$$H_s\{\psi\} = \int d\mathbf{r} \left(-\frac{\tau}{2} \psi^2 + \frac{u}{4} \psi^4 + \frac{K}{2} (\nabla \psi)^2 \right), \quad (3)$$

$$H_l\{\psi\} = \frac{B}{2} \int d\mathbf{r} \int d\mathbf{r}' \psi(\mathbf{r}, t) G(\mathbf{r} - \mathbf{r}') \psi(\mathbf{r}', t), \quad (4)$$

where G is the Green's function for the Laplace equation

$$\nabla_{\mathbf{r}}^2 G(\mathbf{r} - \mathbf{r}') = -\delta(\mathbf{r} - \mathbf{r}'). \quad (5)$$

The above $H\{\psi\}$ is essentially the effective Hamiltonian first derived by Leibler [11] and subsequently discussed by Ohta and Kawasaki [12]. The positive constants M , τ , u , K , and B are phenomenological parameters. Mesoscopic order is caused by competition between short-range attractive and long-range repulsive interactions. They are represented, respectively, by the parameters K in H_s and B in H_l . Hence $H_l\{\psi\}$ is inherent in the microphase separation.

The velocity field $\mathbf{v}(\mathbf{r}, t)$ that advects the field ψ , slowly varying with horizontal coordinates $\mathbf{r}=(x, y)$, is an additional degree of freedom that qualitatively changes the physics [13]. The velocity \mathbf{v} is defined in terms of the vertical vorticity $\Omega \equiv \hat{\mathbf{z}} \cdot \nabla \times \mathbf{v}$ ($\hat{\mathbf{z}}$ being the unit vector along the z axis), which in turn is driven by distortions of the field ψ . We report here results for the same form of vorticity driving used in Ref. [13];

$$\eta_0 (c^2 - \nabla^2) \Omega = \hat{\mathbf{z}} \cdot \left(\nabla \frac{\delta H\{\psi\}}{\delta \psi} \times \nabla \psi \right), \quad (6)$$

where η_0 and c^2 are other phenomenological parameters that determine the strength of the coupling between the hydrodynamic flow and ψ .

Let us introduce the vertical vorticity potential ζ , defined by $\Omega = -\nabla^2 \zeta$, so that $\mathbf{v} = (\partial_y \zeta, -\partial_x \zeta)$. Also hereafter we will use the units in which $u = K = M = 1$. Our model then reads

$$\partial_t \psi = \nabla^2 (-\tau \psi + \psi^3 - \nabla^2 \psi) - B \psi - (\mathbf{v} \cdot \nabla) \psi, \quad (7)$$

$$(c^2 - \nabla^2) \nabla^2 \zeta = g \hat{\mathbf{z}} \cdot [\nabla (\nabla^2 + B \nabla^{-2}) \psi \times \nabla \psi], \quad (8)$$

with $\nabla \cdot \mathbf{v} = 0$, and $g \equiv 1/\eta_0$. In Eq. (8), $\nabla^{-2} \psi$ is a short-hand notation for $-\int d\mathbf{r}' G(\mathbf{r} - \mathbf{r}') \psi(\mathbf{r}')$.

B. CDS modeling

In order to simulate Eqs. (7) and (8), we employed the CDS method on a square lattice [10]. Explicitly, we solved the following CDS model [13–15].

$$\begin{aligned} \psi(n, t+1) &= \psi(n, t) - \langle\langle \mathcal{J}(n, t) \rangle\rangle + \mathcal{J}(n, t) - B \psi(n, t) \\ &\quad - \mathbf{v}(n, t) \cdot [\nabla]_d \psi(n, t), \end{aligned} \quad (9)$$

$$\begin{aligned} (c^2 - [\nabla^2]_d) [\nabla^2]_d \zeta &= g \hat{\mathbf{z}} \cdot \{ [\nabla]_d \{ D(\langle\langle \psi \rangle\rangle - \psi) + B[\nabla^2]_d \psi \} \\ &\quad \times [\nabla]_d \psi \}. \end{aligned} \quad (10)$$

Here $\psi(n, t)$ is the order parameter in the n th cell at time t , and

$$\mathcal{J} \equiv A \tanh \psi + D(\langle\langle \psi \rangle\rangle - \psi) - \psi \quad (11)$$

is the effective chemical potential corresponding to $-\delta H\{\psi\}/\delta \psi$. The parameters A and D set the units used in the CDS dynamics, and the double angular brackets denote an isotropized average of a neighborhood of cells:

$$\begin{aligned} \langle\langle X \rangle\rangle &= \frac{1}{6} \sum X(\text{nearest-neighbor cells}) \\ &\quad + \frac{1}{12} \sum X(\text{next-nearest-neighbor cells}). \end{aligned} \quad (12)$$

In the above equations $[\mathcal{O}]_d$ denotes the discrete version of the enclosed operator \mathcal{O} ; the discrete gradient was center difference evaluated and for the Laplacian we used the identification [16]: $[\nabla^2]_d \mathcal{O} = 3(\langle\langle \mathcal{O} \rangle\rangle - \mathcal{O})$. The operator $[\nabla^{-2}]_d$ is the inverse of the discrete Laplacian $[\nabla^2]_d$, and is computed using fast Fourier transform techniques.

The linear stability analysis of Eq. (9) shows that the homogeneous state ($\psi=0$) is destabilized for

$$A \geq A_c \equiv 1 + 2\sqrt{DB}. \quad (13)$$

The wave number k_m of the most unstable mode is given via the equation

$$2J_0(k_m) + J_0(\sqrt{2}k_m) = 3[1 + (1-A)/(2D)], \quad (14)$$

where J_0 is the Bessel function of the first kind. One also finds from the linear analysis that the wave number k_e that minimizes the free energy, is obtained as the solution of

$$2J_0(k_e) + J_0(\sqrt{2}k_e) = 3(1 - \sqrt{B/D}). \quad (15)$$

III. NUMERICAL RESULTS

We have simulated Eqs. (9) and (10) on a system of size 1024×1024 with periodic boundary conditions. The initial conditions were a random distribution of ψ of amplitude 0.1. The parameters used were $A = 1.22$, $D = 0.45$, $c^2 = 2$, and $B = 0.02$, so that the critical value of A is $A_c = 1.19$, and $k_m = 0.89$, $k_e = 0.82$. Thus the aspect ratio Γ as defined by the system length versus $2\pi/k_e$ is $\Gamma = 134$, and experience has shown that one sample is sufficient to discern the gross behavior of our interest. We also note that the characteristic length scale at late stages of coarsening was found to be one order of magnitude smaller than the system size (see below). Hence we believe that the finite size effects are negligible in our simulations. We will present results for $g = 0$ and $g = 5$ to assess the importance of the hydrodynamic interactions since

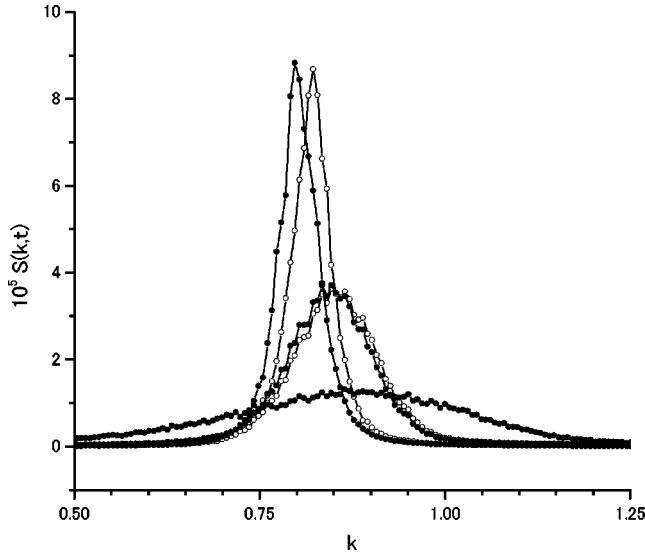


FIG. 1. Time evolution of the circularly averaged scattering function $S(k,t)$ for lamellar formation with (●) and without (○) hydrodynamic coupling. The times are $t=100$, 1000 , and $50\,000$ from low to high peaks, and the scale of the vertical axis is in arbitrary units.

a different growth law may be at work for a higher value of g at which the spiral structure is expected to form [13].

A. Scattering function

We computed the circularly averaged scattering function $S(k,t)$ defined by

$$S(k,t) = \langle \tilde{\psi}(\mathbf{k},t) \tilde{\psi}^*(\mathbf{k},t) \rangle, \quad (16)$$

where $\tilde{\psi}(\mathbf{k},t)$ is the Fourier transform of the order parameter, and the orientation of the wave vector \mathbf{k} is averaged over. To remove any effect due to the finiteness of the ratio of the thickness of domain walls to the domain size, we calculated $S(k,t)$ after the data were hardened using the transformation $\psi \rightarrow \text{sgn}\psi$.

Time evolution of $S(k,t)$ is shown in Fig. 1. It is seen that there is a shift in the position where $S(k,t)$ has its maximum, the shift occurring from k_m toward k_e with increasing time. After the peak had shifted to the position k_e , representing the equilibrium lamellar thickness, narrowing of the scattering profile and the concomitant increase of the peak intensity occurred gradually. It turns out that the latter time region is the region where the scaling behavior of coarsening is observed. We fitted $S(k,t)$ to a squared Lorentzian form

$$S(k,t) = a^2 / [(k^2 - b)^2 + c^2]^2, \quad (17)$$

and extracted the full width at half maximum, $\delta k(t) = \sqrt{\sqrt{2}-1}c/b$, and the peak height, $S_p(t) = a^2/c^4$ of the scattering function at time t . The characteristic length scale (domain size), $\ell(t)$, may then be defined by $\ell(t) = 2\pi/\delta k(t)$. Figure 2 displays the time dependence of the peak intensity and width measured in this way. The characteristic length scale is well fitted by a power law $\ell \sim t^\alpha$ with

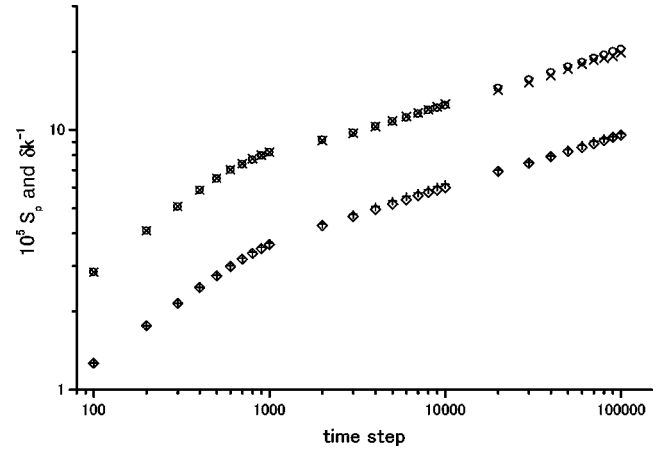


FIG. 2. Time evolution of the peak intensity S_p (bottom) and the inverse of the width δk (top) of the scattering function for lamellar formation. Open symbols are data for $g=0$ while crosses are for $g=5$.

$\alpha = 0.20 \pm 0.01$. The peak height also grows as a power law: $S_p \sim t^\beta$ and we found $\beta = \alpha$. The result $\alpha = \beta$ implies that $S(k,t)$ satisfies the scaling $S(k,t) = \ell(t)f((k-k_e)\ell(t))$, where $f(x)$ is a scaling function. The notable feature of the result demonstrated by Fig. 2 is that we have a same scaling consistent with $\ell \sim t^{1/5}$ with the inclusion of hydrodynamic couplings.

B. Orientational correlation function

However, the morphology of the patterns appears rather different in the presence and absence of hydrodynamics (see Fig. 3). If hydrodynamics is included, it enhances removal of defects and lamellae smoothly curved are evident in the figure. To quantify the difference we have calculated the temporal change in orientation of the lamellae.

A direct method of probing the orientational order is to evaluate a correlation function of the local orientation field, $\theta(\mathbf{r},t)$, of the lamellar patterns. Explicitly, we have computed the correlation function

$$C_2(R,t) \equiv \langle \exp\{2i[\theta(\mathbf{r}+\mathbf{R},t) - \theta(\mathbf{r},t)]\} \rangle \quad (18)$$

averaging over the spatial coordinate \mathbf{r} and \mathbf{R} for fixed $R \equiv |\mathbf{R}|$. The local orientation θ is defined as the angle in the direction normal to the lamellar axis. The factor of 2 is required by a twofold symmetry of lamellar patterns, We have employed the prescription described in Appendix A to extract θ from simulation data. Figure 4(a) shows $C_2(r,t)$ for $g=0$ at various times. The correlation decays with increasing separation r , and from this decay we can extract the orientational correlation length $\xi_h(t)$ as the value of r at which $C_2(r,t)$ reaches the value of h , where $h(<1)$ is some constant [note that $C_2(0,t)=1$]. The scaling exponent γ is extracted from a log-log plot of $\xi_h(t)$ versus time. As shown in Fig. 4(b), γ assumes the same value independent of h , hence in the following we choose to use simply $\xi_{1/2}(t)$ as a characteristic length [which we now denote by $\xi(t)$] of the orientation field.

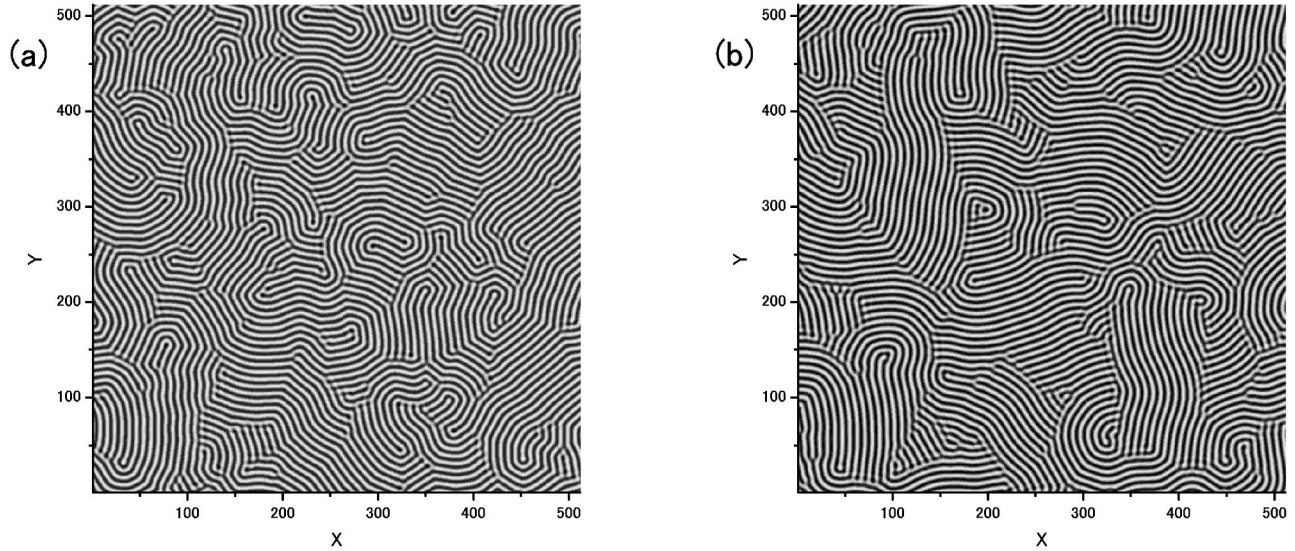


FIG. 3. Lamellar patterns achieved at $t=10^5$ for $g=0$ (a) and 5 (b) with the same initial condition. The bright regions correspond to positive values of the order parameter ψ while the dark ones to negative ψ . Each figure exhibits a 512^2 portion of the 1024^2 lattice result.

As might be expected, the qualitative difference observed in Fig. 3 is magnified through the orientation field. See Fig. 5. The $\xi(t)$ is consistent with the power law $\xi \sim t^\gamma$. We found $\gamma=0.21 \pm 0.01$ for $g=0$ and $\gamma=0.30 \pm 0.01$ for $g=5$, confirming the stronger orientational growth in the presence of hydrodynamic flow.

IV. HYDRODYNAMIC INTERACTIONS IN HEXAGONAL PATTERNS

The lamellar phase is stable for nearly symmetric diblocks, while a hexagonally packed phase is stable for diblocks with intermediate levels of compositional asymmetry. Increasing the volume fraction (or block ratio f) of A blocks, say $f > 1/2$, induces interfacial curvature allowing the longer A blocks to reside on the convex side of the A - B interface, thus reducing the elastic energy.

Hexagons are equivalent to superposition of three lamel-

lae aligned at multiples of $\pi/3$. However, the hexagonal pattern has several features that sharply define it from the lamellar pattern. A perfectly regular hexagonal pattern is not permitted in a square box or any box with rational aspect ratio because the structure has to fit with nonmatching boundary conditions such as periodic boundary conditions. The so-called penta-hepta defects, most typical point defects in hexagonal patterns, are very stable once having been created [17]. It is with good reasons, therefore, to ask whether coarsening of the hexagonal pattern is governed by the same growth law as found in the case of lamellar systems.

A. Model equations

It is now widely recognized that the hexagonal structures are described by a simple extension of the free energy (4) in the form [12]

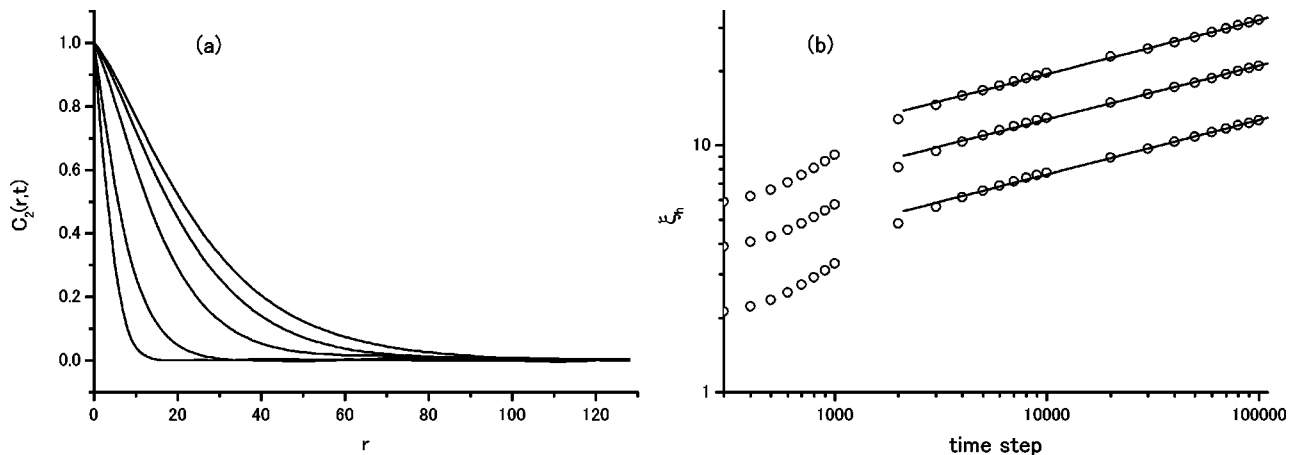


FIG. 4. (a) Time evolution of the orientational correlation function $C_2(r,t)$ in the absence of hydrodynamic flow with successive time steps; $t=10^2, 10^3, 10^4, 5 \times 10^4$, and 10^5 increasing from left to right. (b) Time evolution of the length scale $\xi_h(t)$ for which $C_2(\xi_h, t) = h$, where $h=0.3, 0.5, 0.7$ from top to bottom. Lines of best fit to data are also drawn, and all have the same slope 0.21.

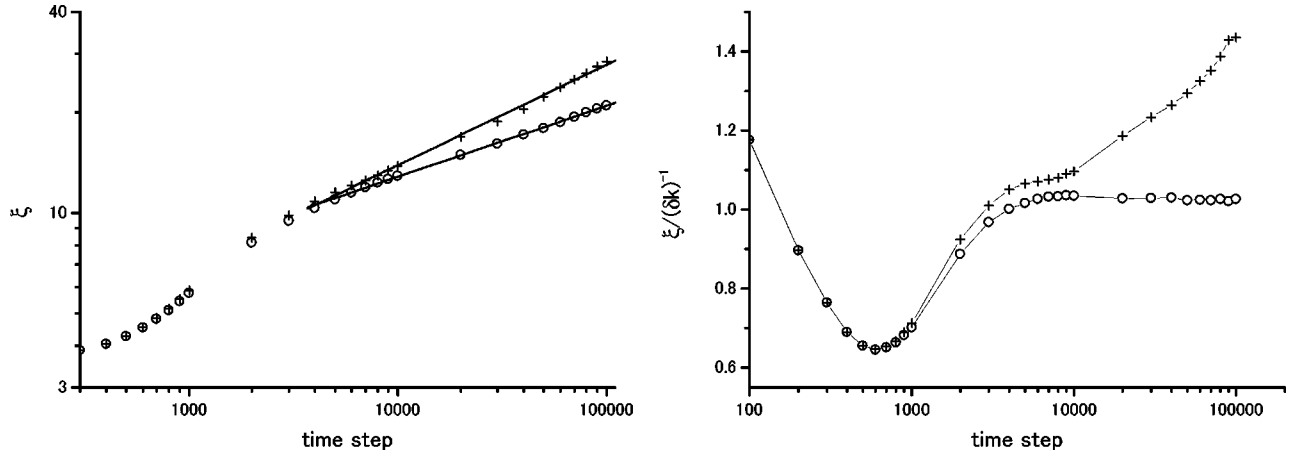


FIG. 5. Time evolution of the half width ξ of the orientational correlation function $C_2(r,t)$. Open symbols denote the result for $g=0$ while crosses are for $g=5$. Lines of the best fit to data are also drawn. Shown on the right is the plot of $\xi/(\delta k)^{-1}$ versus t where δk is the width of the scattering function.

$$H_{\Gamma}\{\psi\} = \frac{B}{2} \int d\mathbf{r} \int d\mathbf{r}' \delta\psi(\mathbf{r},t) G(\mathbf{r}-\mathbf{r}') \delta\psi(\mathbf{r}',t), \quad (19)$$

where $\delta\psi(\mathbf{r},t) = \psi(\mathbf{r},t) - \bar{\psi}$ with $\bar{\psi}$, the spatial average of $\psi(\mathbf{r})$, given by $\bar{\psi} = 2f - 1$. The only changes caused by the replacement (19) in the model are substitutions:

$$B\psi \rightarrow B(\psi - \bar{\psi}) \quad \text{in Eq. (7),}$$

$$B\psi(n,t) \rightarrow B(\psi(n,t) - \bar{\psi}) \quad \text{in Eq. (9).}$$

Thus

$$A \rightarrow A \operatorname{sech}^2 \bar{\psi} \quad \text{in Eqs. (13) and (14),}$$

$$\bar{\psi}(\mathbf{k},t) \rightarrow \delta\bar{\psi}(\mathbf{k},t) \quad \text{in Eq. (16).}$$

With these changes coarsening of hexagonal patterns has been simulated and the time evolution of the field ψ is now given in below.

B. Simulations

We have studied the hexagonal domain coarsening for $\bar{\psi} = -0.2$, which corresponds to $f=0.4$. In the simulations we chose $A = 1.25$ since the dynamics appears to freeze at long times for higher values. All the other parameters and the initial conditions are the same as in Sec. III.

The scattering functions at several time steps are shown in Fig. 6(a). In Fig. 6(b) the semilogarithmic plot of $S(k,t)$ versus k at higher wave numbers, the second and third peaks are evident. In particular, the peak at $k \approx \sqrt{3}k_e$ (k_e being the primary peak position) is related to the development of (110) planes of the hexagonal phase. Figure 7 displays a double-logarithmic plot of the width $\delta k(t)$ and the peak intensity

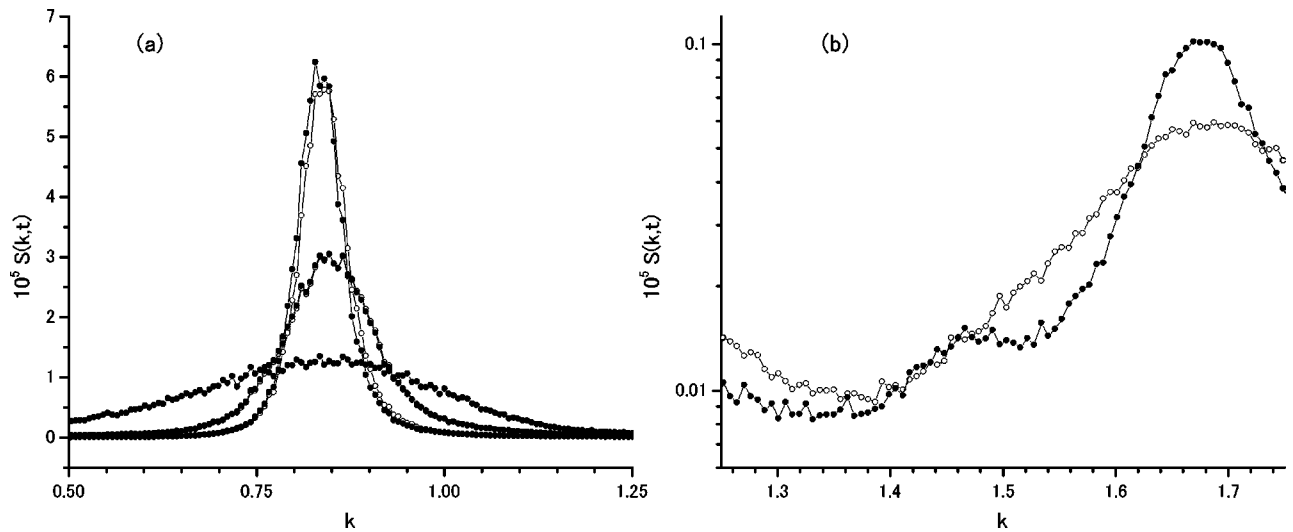


FIG. 6. (a) Time evolution of the scattering function $S(k,t)$ for hexagonal pattern formation with (●) and without (○) hydrodynamic coupling. The times are $t=100, 1000$, and $50\,000$ from low to high peaks, and $S(k,t)$ is in arbitrary units. (b) The higher-order peaks of $S(k,t)$ for the case $g=5$ at $t=6000$ (○) and 10^5 (●). Notice of the logarithmic scale of the vertical axis.

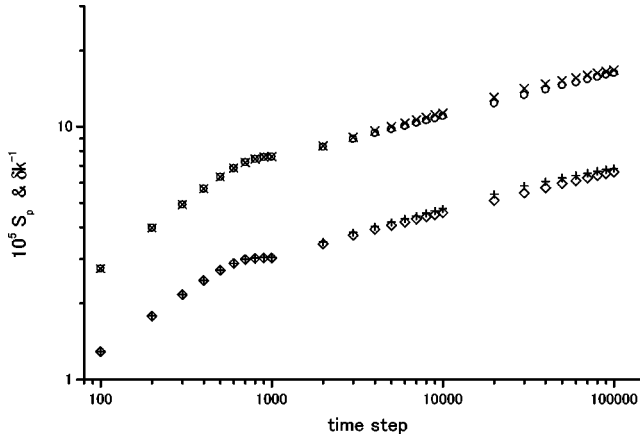


FIG. 7. Time evolution of the peak intensity S_p (bottom) and the inverse of the width δk (top) of the scattering function for hexagonal formation. Open symbols are data for $g=0$ while crosses are for $g=5$.

$S_p(t)$ of $S(k,t)$ versus time. The growth behaviors with and without inclusion of hydrodynamics display very little difference. The time dependence of δk and of S_p obey the power law $\delta k^{-1} \sim t^\alpha$ and $S_p \sim t^\beta$ with $\alpha = \beta = 0.17 \pm 0.01$, roughly consistent with the $t^{1/5}$ scaling for lamellar growth.

In Fig. 8(a) we demonstrate the hexagonal pattern attained at $t=10^5$ for $g=5$. The corresponding morphology for $g=0$ is not shown there because a big difference was hardly visible through the eye. One can then wonder whether the distinction between the absence and the presence of hydrodynamic coarsening is marked in the orientational order in hexagonal structures. Since the order is in the orientation of domains aligned at multiples of $\pi/3$, the appropriate correlation function to look at is

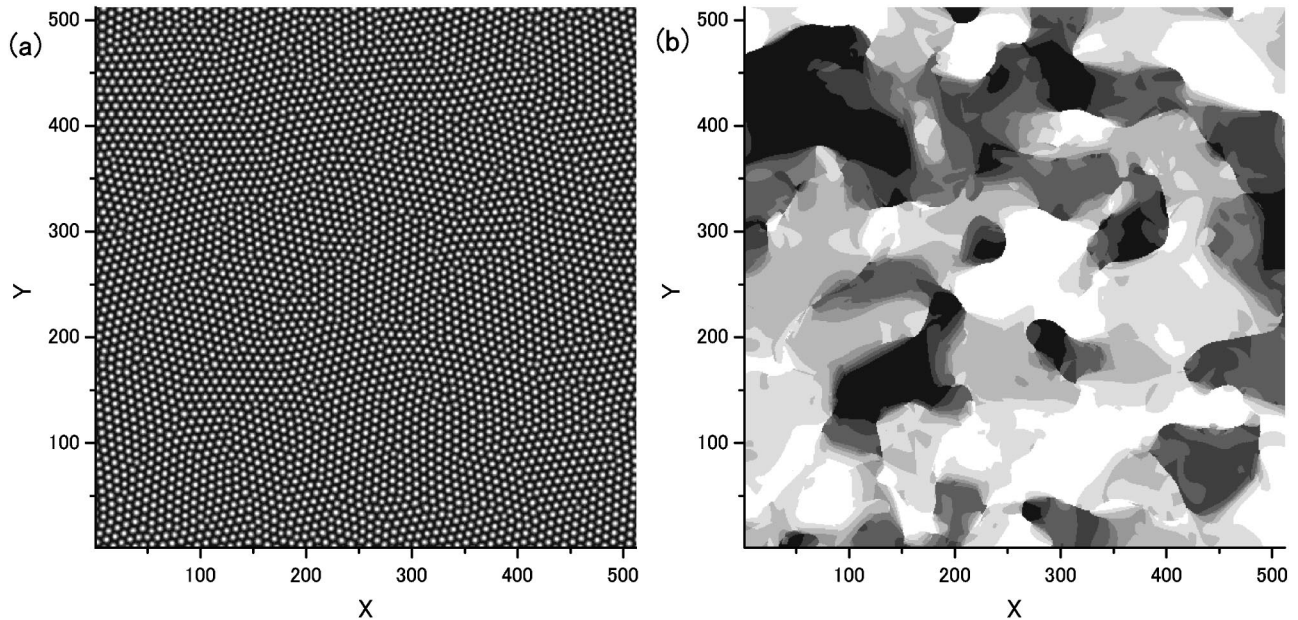


FIG. 8. (a) Hexagonal pattern achieved at $t=10^5$ in the presence of hydrodynamic coupling. The bright regions denote positive values of ψ while dark ones denote negative ψ . The corresponding orientation field $\theta(\mathbf{r})$ is displayed on the panel (b). It is displayed by plotting $\cos 6\theta(\mathbf{r})$ with eight gray levels; the bright regions correspond to regions with $\cos 6\theta > 0$ and the dark ones denote $\cos 6\theta < 0$. Both panels exhibit a 512^2 portion of the 1024^2 system.

$$C_6(R,t) \equiv \langle \exp\{6i[\theta(\mathbf{r}+\mathbf{R},t) - \theta(\mathbf{r},t)]\} \rangle. \quad (20)$$

The right panel (b) in Fig. 8 displays the orientation field $\theta(\mathbf{r})$ of the pattern of the left panel. We have plotted there $\cos 6\theta(\mathbf{r})$ with eight gray levels.

We have extracted the orientational characteristic length $\xi(t)$ by calculating $C_6(r,t)$ with the same method that we used for $C_2(r,t)$. The result is shown in Fig. 9. The exponent γ for ξ is estimated from the straight line fit to be $\gamma = 0.20 \pm 0.01$ for two cases (i.e., $g=0$ and 5). Thus even with the addition of hydrodynamic flow the growth remains consistent with the $t^{1/5}$ scaling in the hexagonal formation.

V. SUMMARY AND DISCUSSION

The first theoretical attempt to study the role of hydrodynamic interactions in the formation of a mesophase of block copolymers was by Bahiana and Oono [15]. Using the CDS approach, they tried to get over the difficulty in producing a well-aligned lamellar structure when the velocity field is absent. Later Gonnella *et al.* [6] addressed the problem using lattice Boltzmann simulations. These works find that the hydrodynamic fields allow the lamellae to reorder giving locally well-defined lamellar regions.

So far, however, the dynamical growth of the characteristic length scale $L(t)$ in the pattern dynamics has not been studied in the presence of hydrodynamic interactions. The single exception is a numerical study in Ref. [7], where the authors have measured $L(t)$ by the location of the first zero of the pair correlation function of the order parameter. However, the system saturated at quite earlier time (supposedly due to the small system size used in the simulation), and owing to the lack of data for large time the scaling growth is

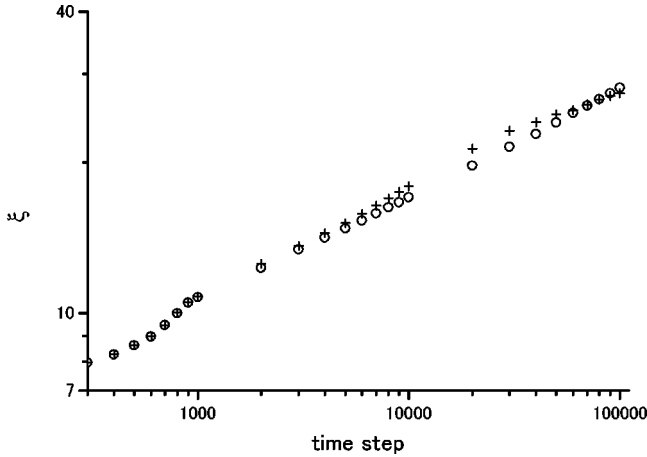


FIG. 9. Time evolution of the half width ξ of the orientational correlation function $C_6(r, t)$ for hexagonal pattern formation with (+) and without (○) hydrodynamics.

not convincingly demonstrated. Recent numerical work by Maurits *et al.* [8] and by Groot *et al.* [9] focused on the following quantities:

$$\omega(t) \equiv V^{-1} \int d\mathbf{r} \delta\psi^2(\mathbf{r}, t), \quad p(t) \equiv \sum_{\mathbf{k}} S(\mathbf{k}, t) \ln S(\mathbf{k}, t), \quad (21)$$

where V is the system volume. Unfortunately, by definition these parameters cannot contain the characteristic length scale, hence fail to capture the essential features of the ordering dynamics. In this connection it is worth adding that the power-law scaling is always observed after the $\omega(t)$ reaches the final plateau corresponding to its equilibrium value. [In Ref. [8], the authors also studied the time dependence of the scattering function $S(k, t)$. They then identified the lower value of the peak position (k_p) of $S(k, t)$ with the larger domain size. However, k_p does not represent the domain size but instead the lamellar spacing, being of no direct relevance to coarsening kinetics.]

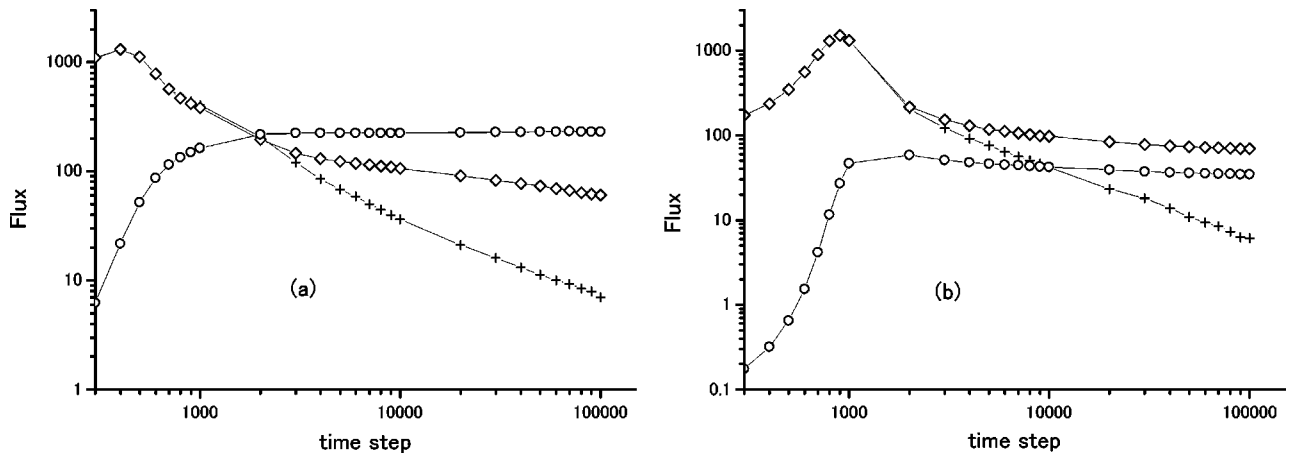


FIG. 10. Temporal change in the average hydrodynamic flux \mathcal{F}_h (○) and the average diffusion flux \mathcal{F}_d (crosses denote \mathcal{F}_d for $g=0$ and diamonds for $g=5$) in the coarsening of lamellar (a) and hexagonal (b) domains.

We have given in this paper a detailed numerical analysis of the growth law of domain coarsening. The conclusions that we can draw from the present simulations are as follows.

(1) With hydrodynamic interactions the lamella-forming system removes its topological defects more effectively, enhancing the lamellar orientation.

(2) The flow-enhanced orientation is reflected in the increased growth exponent of the characteristic length for the asymptotic orientational order.

(3) The power-law growth for the hexagonal domain coarsening shows very little difference with the inclusion of hydrodynamic interactions.

To understand the underlying cause of the difference between lamellar and hexagonal domain coarsenings, we show in Fig. 10 the temporal change in the strength of the hydrodynamic flux (\mathcal{F}_h) and the dissipative or diffusion flux (\mathcal{F}_d). They are defined, respectively, by

$$\mathcal{F}_h/V \equiv \langle |\psi \mathbf{v}| \rangle, \quad (22)$$

$$\mathcal{F}_d/V \equiv \left\langle \left| -\nabla \frac{\delta H}{\delta \psi} \right| \right\rangle. \quad (23)$$

Comparing the relative importance of the two transport mechanisms seen in Fig. 10(a) in combination with Fig. 5, we can deduce that the hydrodynamic flow is responsible for the increased orientational order in lamellar patterns. In fact, the orientational characteristic length ξ starts growing faster than the other length scale ℓ (δk^{-1}) once the hydrodynamic flux becomes dominant. In this sense it is well justified that the hydrodynamic process in coarsening is sometimes referred to as geometrical coarsening [18] since it does not accompany the acceleration of the length scale ℓ , which is probed by the density correlation function $S(k, t)$. Hence the late-stage coarsening of lamellar phases cannot be universally described by a single power law, and probably depends on the strength of hydrodynamic coupling. To investigate the latter point systematically, is left for a future study. In this context, it would be extremely fruitful to pursue an analogy [4,19] between pattern dynamics of the lamellar phase and

that of a roll state observed in Rayleigh-Bénard convections for which some amount of data are now accumulating [20].

Contrary to the lamellar case, the hydrodynamic field in the hexagonal pattern formation is playing a subdominant role and is not strong enough to alter the growth law. The diffusion flux is always dominant throughout the late stage of coarsening [see Fig. 10(b)]. Although we studied several systems with combinations of the model parameters other than presented in the preceding section, we found no indication that \mathcal{F}_h becomes dominant over \mathcal{F}_d . It is not yet understood why hydrodynamic flux cannot be equally important for asymmetric block copolymers, and it will be of great interest to further investigate this problem.

Finally we briefly touch upon the wave number selection. In our simulations we found that the peak position of the scattering function reaches a constant value at $t \approx 10\,000$ and remains at that value thereafter. Obviously the system selects a particular wave number for periodic structures in rather earlier stages of pattern formation. (Recall the results in Secs. III and IV that the power-law scaling of the domain size is observed in much late stages.) Furthermore, the selected wave number of the lamellar phase is decreased when the hydrodynamic interactions are present, as seen from Fig. 1. A possible explanation of this fact is beyond the scope of the present paper because wave number adjustment might involve the spatial inhomogeneities induced by defects; and the understanding of defect motion in the coarsening process remains challenging [21]. Notwithstanding this, we apply a random phase approximation to solve our model. The analysis is given in Appendix B. It is shown there that the nonlinearity induced by hydrodynamic couplings leads to the stationary pattern of smaller wave numbers. However, it is unclear whether this is the dominant mechanism of the wave number selection problem in block copolymer systems.

APPENDIX A: DOMAIN ORIENTATION FIELD

In this appendix we describe a technique to extract the domain orientation field (to be referred to as a director field hereafter), $\theta(\mathbf{r})$, of the domain structure. To construct the director field we cannot use the local gradient of the order parameter field $\psi(\mathbf{r})$ since it vanishes at maximum and minimum of $\psi(\mathbf{r})$. Instead we use a slight modification of the Fourier space filtering method of Ref. [22]. For ease of understanding of this technique, we first consider the lamellar patterns.

An important observation to implement the method is that $S(k) = \langle \tilde{\psi}(\mathbf{k}) \tilde{\psi}^*(\mathbf{k}) \rangle$ [$\tilde{\psi}(\mathbf{k})$ being the Fourier transform of $\psi(\mathbf{r})$] for each time t is strongly peaked at $k = k_p$ (which is time dependent, in general). We thus introduce a filtering operator \mathcal{F}_σ that reduces the amplitude of the components $\tilde{\psi}(\mathbf{k})$ that lie off the $k = k_p$ ring in Fourier space. For simplicity we choose a Gaussian filter, so that the filtering is defined by

$$\mathcal{F}_\sigma \psi(\mathbf{r}) = \psi_f(\mathbf{r}, \theta_f) \equiv \int_{\mathbf{k}} e^{-i\mathbf{k} \cdot \mathbf{r}} e^{-(\mathbf{k} - \mathbf{k}_f)^2 / \sigma^2} \tilde{\psi}(\mathbf{k}), \quad (\text{A1})$$

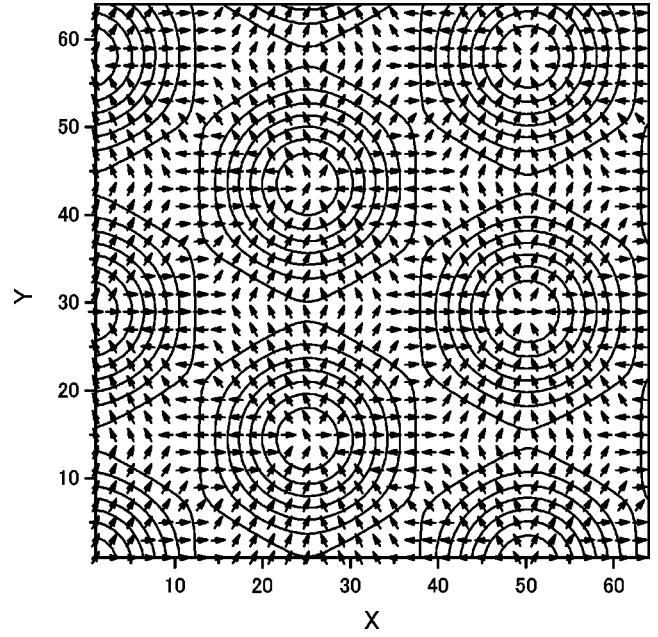


FIG. 11. Orientation field $\theta(\mathbf{r})$ of the equilateral hexagonal structure [given by Eq. (A4) with $k_p = 1/4$] as obtained by the filtered Fourier transform method. The unit vector at site \mathbf{r} denotes the angle $\theta(\mathbf{r})$, and a contour plot of the hexagonal pattern is also displayed.

where $\mathbf{k}_f = k_p(\cos \theta_f, \sin \theta_f)$, and σ sets the width of the filtering. The filtered function $\psi_f(\mathbf{r}, \theta_f)$ is large in magnitude in those domains where the direction normal to the local lamella is close to the θ_f direction. We then define the director field $\theta(\mathbf{r})$ at each point \mathbf{r} as the angle maximizing $|\psi_f(\mathbf{r}, \theta_f)|$ as a function of θ_f .

To convince oneself of the algorithm, take up an ideal state of straight parallel lamellae:

$$\psi(\mathbf{r}) = A \cos(k_p x). \quad (\text{A2})$$

Then

$$|\psi_f(\mathbf{r}, \theta_f)|^2 = (A^2/2) e^{-4(k_p/\sigma)^2} \{ \cosh[4(k_p/\sigma)^2 \cos \theta_f] + \cos(2k_p x) \}. \quad (\text{A3})$$

Finding the angle maximizing $|\psi_f(\mathbf{r}, \theta_f)|$, one obtains $\theta(\mathbf{r}) = 0$ at any \mathbf{r} , as required.

The above method works equally well for the hexagons because superposition of three straight lamellae aligned at multiples of $\pi/3$ is equivalent to the hexagonal pattern. To illustrate this, we show in Fig. 11 the ideal pattern of hexagons,

$$\psi(\mathbf{r}) = \frac{1}{2} \sum_{j=1}^3 (e^{i\mathbf{k}_j \cdot \mathbf{r} + c.c.}), \quad (\text{A4})$$

where $\mathbf{k}_1 = k_p(1, 0)$, $\mathbf{k}_2 = k_p(-1/2, \sqrt{3}/2)$, and $\mathbf{k}_3 = k_p(-1/2, -\sqrt{3}/2) = -(\mathbf{k}_1 + \mathbf{k}_2)$, together with the director field $\theta(\mathbf{r})$ that we have numerically extracted by the filtering algorithm. (In the actual numerical calculations we have used eight

angles of θ_f equally spaced around the semicircle at $k=k_p$ with $\sigma=0.15$, and fit a parabola to sets of three neighboring points to determine the maximum.) If we note a sixfold degeneracy of the ideal hexagons, then it can be seen that the algorithm correctly captures the domain structure; i.e., θ is equal to Bragg angle of the two-dimensional triangular Bravais lattice [23].

APPENDIX B: STATIONARY WAVE NUMBER WITH ADDED FLOW

In this appendix we consider how the presence of the hydrodynamic coupling affects the preferred wave number of the final stationary lamellar states. We start with Eqs. (7) and (8):

$$\partial_t \psi = [\epsilon - (\nabla^2 + k_0^2)] \psi + \tilde{g} \nabla^2 \psi^3 - (\mathbf{v} \cdot \nabla) \psi, \quad (\text{B1})$$

$$\nabla^2 \zeta = g \hat{\mathbf{z}} \cdot [\nabla(\nabla^2 + B \nabla^{-2}) \psi \times \nabla \psi], \quad (\text{B2})$$

with $\mathbf{v} = (\partial_y \zeta, -\partial_x \zeta)$, where we have rewritten Eq. (7) with

$$\epsilon \equiv (\tau^2/4) - B, \quad k_0 \equiv \sqrt{\tau/2}. \quad (\text{B3})$$

Since $-\nabla^2 \zeta / c^2 \zeta \sim h^2 / L^2 \ll 1$ [13] where h is the vertical thickness of the system and L is the horizontal characteristic length, we have neglected, for simplicity, the ∇^2 term on the left-hand side of Eq. (8) [hence $g \equiv 1/(c^2 \eta_0)$ in Eq. (B2)]. In Eq. (B1) we have inserted the nonlinear coupling parameter \tilde{g} for convenience, which is eventually set $\tilde{g} = 1$. Notice that the form (B1) is very similar to the Swift-Hohenberg (SH) equation [24], which is a model describing cellular pattern formation in Rayleigh-Bénard convection. The only difference of Eq. (B1) from the SH equation is the existence of a positive definite operator $-\nabla^2$ in front of the nonlinear term.

Let us solve Eqs. (B1) and (B2) in Fourier space. We define the Fourier transformation of an arbitrary function $f(\mathbf{r})$ as $f(\mathbf{r}) = \sum_{\mathbf{k}} f(\mathbf{k}) e^{i\mathbf{k} \cdot \mathbf{r}}$, where the same notation f in Fourier space should not cause any confusion hereafter. It is easy to solve Eq. (B2) for $\zeta(\mathbf{k})$, with which Eq. (B1) is cast into the following form after some algebra:

$$\begin{aligned} \partial_t \psi(\mathbf{k}) &= r(k) \psi(\mathbf{k}) - \tilde{g} k^2 \sum_{\mathbf{k}_1} \sum_{\mathbf{k}_2} \psi(-\mathbf{k}_1) \psi(\mathbf{k}_2) \\ &\quad \times \psi(\mathbf{k} + \mathbf{k}_1 - \mathbf{k}_2) - g V(\mathbf{k}), \end{aligned} \quad (\text{B4})$$

where

$$r(k) = \epsilon - (k^2 - k_0^2)^2. \quad (\text{B5})$$

The last term on the right-hand side (RHS) of Eq. (B4) is the flow contribution, and

$$V(\mathbf{k}) = \sum_{\mathbf{k}_1} \sum_{\mathbf{k}_2} v(\mathbf{k}; \mathbf{k}_1, \mathbf{k}_2) \psi(-\mathbf{k}_1) \psi(\mathbf{k}_2) \psi(\mathbf{k} + \mathbf{k}_1 - \mathbf{k}_2) \quad (\text{B6})$$

with

$$\begin{aligned} v(\mathbf{k}; \mathbf{k}_1, \mathbf{k}_2) &\equiv \frac{1}{2} \frac{\hat{\mathbf{z}} \cdot [\mathbf{k} \times (\mathbf{k}_2 - \mathbf{k}_1)] \hat{\mathbf{z}} \cdot (\mathbf{k}_2 \times \mathbf{k}_1)}{|\mathbf{k}_2 - \mathbf{k}_1|^2} \\ &\quad \times \left(k_1^2 + \frac{B}{k_1^2} - k_2^2 - \frac{B}{k_2^2} \right). \end{aligned} \quad (\text{B7})$$

It should be remarked that the hydrodynamic coupling $g v(\mathbf{k}; \mathbf{k}_1, \mathbf{k}_2)$ is strictly zero if all the wave vectors \mathbf{k} allowed in $\psi(\mathbf{k})$ lie on one single ring $|\mathbf{k}| = k_e$, corresponding to either an infinite system of lamellae parallel to, say, x direction or axisymmetric lamellar patterns.

In this appendix, we will focus on the scattering function defined by

$$S(k, t) = \langle J(\mathbf{k}, t) \rangle, \quad J(\mathbf{k}, t) \equiv \psi(\mathbf{k}, t) \psi^*(\mathbf{k}, t).$$

From Eq. (B4) we get

$$\begin{aligned} \partial_t J(\mathbf{k}, t) &= 2r(k) J(\mathbf{k}, t) - \sum_{\mathbf{k}_1} \sum_{\mathbf{k}_2} \{ [\tilde{g} k^2 + g v(\mathbf{k}; \mathbf{k}_1, \mathbf{k}_2)] \\ &\quad \times \psi(-\mathbf{k}, t) \psi(-\mathbf{k}_1, t) \psi(\mathbf{k}_2, t) \psi(\mathbf{k} + \mathbf{k}_1 - \mathbf{k}_2, t) \\ &\quad + (\mathbf{k} \rightarrow -\mathbf{k}) \}, \end{aligned} \quad (\text{B8})$$

where $(\mathbf{k} \rightarrow -\mathbf{k})$ means a replacement in the foregoing term. In order to proceed to find the equation for $S(k, t)$ we need to calculate the average of the four-point correlation function. For this purpose we notice that the instantaneous patterns we observed in the simulations are labyrinthine and irregular in space. Hence we assume that the four-point correlation is determined entirely by the pair correlation function, and that two modes of different \mathbf{k} 's are poorly correlated. (Note that during the coarsening of lamellar domains under consideration, the averages $\langle \psi(\mathbf{k}, t) \rangle$ are zero, and therefore should not contribute.) Thus we substitute

$$\begin{aligned} \langle \psi(-\mathbf{k}, t) \psi(-\mathbf{k}_1, t) \psi(\mathbf{k}_2, t) \psi(\mathbf{k} + \mathbf{k}_1 - \mathbf{k}_2, t) \rangle \\ \approx \delta_{\mathbf{k}_1, -\mathbf{k}} S(k, t) S(k_2, t) + \delta_{\mathbf{k}_2, \mathbf{k}} S(k, t) S(k_1, t) \\ + \delta_{\mathbf{k}_1, \mathbf{k}_2} S(k, t) S(k_1, t), \end{aligned}$$

which yields

$$\partial_t S(k, t) = 2S(k, t) \left\{ r(k) - \sum_{\mathbf{k}_1} [3\tilde{g} k^2 + g \hat{v}(\mathbf{k}, \mathbf{k}_1)] S(k_1, t) \right\}. \quad (\text{B9})$$

Here

$$\hat{v}(\mathbf{k}, \mathbf{k}_1) = \frac{|\hat{\mathbf{z}} \cdot (\mathbf{k} \times \mathbf{k}_1)|^2}{|\mathbf{k} - \mathbf{k}_1|^2} \left(k^2 + \frac{B}{k^2} - k_1^2 - \frac{B}{k_1^2} \right). \quad (\text{B10})$$

At this juncture, we define the effective response function $\chi(\mathbf{k}, t)$ by writing Eq. (B9) as

$$\partial_t S(k, t) = -2k^2 \chi^{-1}(\mathbf{k}, t) S(k, t) \quad (\text{B11})$$

on the analogy of the relaxation to equilibrium in the general theory of response functions. (A cautionary remark is in order here. Since the dynamical model defined by Eqs. (B1) and (B2) neglects the noise terms, the solution of Eq. (B11) does not relax to the proper equilibrium state. With the noise source included, however, the relationship (B12) below remains unaltered.) Then we find

$$\chi^{-1}(\mathbf{k}, t) = \tilde{\tau}(t) + k^2 + \frac{B}{k^2} + g \sum_{\mathbf{q}} \frac{\hat{v}(\mathbf{k}, \mathbf{q})}{k^2} S(q, t), \quad (\text{B12})$$

where we have used the relations (B5) and (B3), and

$$\tilde{\tau}(t) \equiv 3g \sum_{\mathbf{q}} S(q, t) - \tau.$$

Given this χ , we identify the asymptotic peak position k_e of the scattering function $S(k) \equiv S(k, t \rightarrow \infty)$ with the wave number at which χ achieves its maximum. One finds from Eq. (B12) that k_e is then given by the solution to the following equation:

$$k_e^4 - k_b^4 - g \sum_{\mathbf{q}} \hat{v}(\mathbf{k}_e, \mathbf{q}) S(q) + g k_e^2 \left[\frac{\partial}{\partial k^2} \sum_{\mathbf{q}} \hat{v}(\mathbf{k}, \mathbf{q}) S(q) \right]_{\mathbf{k}=\mathbf{k}_e} = 0, \quad (\text{B13})$$

where we have defined $k_b \equiv B^{1/4}$. Note that in the absence of the flow ($g=0$), Eq. (B13) yields $k_e = k_b$, reproducing a well-known result [12]. Equation (B13) is soluble for small g by substituting

$$S(q) = \frac{1}{\tilde{\tau} + k^2 + B/k^2} \approx \frac{k_b^2}{\hat{\epsilon} + (k^2 - k_b^2)^2} \quad (\text{B14})$$

into the left-hand side of Eq. (B13). Here $\hat{\epsilon} \equiv k_b^2(\tilde{\tau} + 2k_b^2)$, and the last equality follows from the fact that $S(k)$ in this form has a maximum at $k = k_b$. This approximation is valid for sufficiently small $\hat{\epsilon}$. (We can prove *a posteriori* that the renormalized parameter $\hat{\epsilon}$ is always positive.) For small enough $\hat{\epsilon}$, we find that

$$\left[\frac{\partial}{\partial k^2} \sum_{\mathbf{q}} \hat{v}(\mathbf{k}, \mathbf{q}) S(q) \right]_{\mathbf{k}=\mathbf{k}_e} \approx \frac{1}{2} \left(k_e^2 - \frac{k_b^4}{k_e^2} \right) \sum_{\mathbf{q}} S(q),$$

and thus the last term on the LHS of Eq. (B13) contributes at $O(g^2)$ since $k_e = k_b + O(g)$. The remaining term $\sum_{\mathbf{q}} \hat{v}(\mathbf{k}_e, \mathbf{q}) S(q)$ can be evaluated analytically by converting to a continuous Fourier space. We obtain

$$\sum_{\mathbf{q}} \hat{v}(\mathbf{k}_e, \mathbf{q}) S(q) \approx \frac{k_b^4}{4\pi} \ln \left(\frac{\Lambda}{k_b} \right),$$

where Λ is the upper momentum cutoff. Thus we finally get

$$k_e = k_b \left[1 - \frac{\ln(\Lambda/k_b)}{16\pi} g \right] \quad (\text{B15})$$

to the leading order of accuracy. Since $\ln(\Lambda/k_b) \approx \ln(\lambda/d) > 0$, where λ and d are lamellar spacing and domain width, respectively, we see that, in fact, there is a trend to smaller wave numbers at long times with added flow.

-
- [1] For a recent review, see A.J. Bray, *Adv. Phys.* **43**, 357 (1994).
[2] V.M. Kendon, M.E. Cates, I. Pagonabarraga, J-C. Desplat, and P. Bladon, *J. Fluid Mech.* **440**, 147 (2001), and references therein.
[3] F. Liu and N. Goldenfeld, *Phys. Rev. A* **39**, 4805 (1989); A. Chakrabarti, R. Toral, and J.D. Gunton, *ibid.* **44**, 6503 (1991); C. Harrison, D.H. Adamson, Z. Cheng, J.M. Sebastian, S. Sethuraman, D.A. Huse, R.A. Register, and P.M. Chaikin, *Science* **290**, 1558 (2000).
[4] Y. Shiwa, T. Taneike, and Y. Yokojima, *Phys. Rev. Lett.* **77**, 4378 (1996); J.J. Christensen and A.J. Bray, *Phys. Rev. E* **58**, 5364 (1998).
[5] T. Taneike and Y. Shiwa, *J. Phys.: Condens. Matter* **9**, L147 (1999); T. Taneike, T. Nakajima, T. Nihei, and Y. Shiwa (unpublished).
[6] G. Gonnella, E. Orlandini, and J.M. Yeomans, *Phys. Rev. Lett.* **78**, 1695 (1997).
[7] I. Podariu, Z. Shou, and A. Chakrabarti, *Phys. Rev. E* **62**, R3059 (2000).
[8] N.M. Maurits, A.V. Zvelindovsky, G.J.A. Sevink, B.A.C. van Vlimmeren, and J.G.E.M. Fraaije, *J. Chem. Phys.* **108**, 9150 (1998).
[9] R.D. Groot, T.J. Madden, and D.J. Tildesley, *J. Chem. Phys.* **110**, 9739 (1999).
[10] Y. Oono and S. Puri, *Phys. Rev. Lett.* **58**, 836 (1987); *Phys. Rev. A* **38**, 434 (1988); S. Puri and Y. Oono, *ibid.* **38**, 1542 (1988); for more recent references, see A. Shinozaki and Y. Oono, *Phys. Rev. E* **48**, 2622 (1993).
[11] L. Leibler, *Macromolecules* **13**, 1602 (1980).
[12] T. Ohta and K. Kawasaki, *Macromolecules* **19**, 2621 (1986).
[13] Y. Shiwa, *Phys. Rev. E* **61**, 2924 (2000).
[14] Y. Oono and Y. Shiwa, *Mod. Phys. Lett. B* **1**, 49 (1987).
[15] M. Bahiana and Y. Oono, *Phys. Rev. A* **41**, 6763 (1990).
[16] P.I.C. Teixeira and B.M. Mulder, *Phys. Rev. E* **55**, 3789 (1997); Y. Oono, *ibid.* **55**, 3792 (1997).
[17] S. Ciliberto, P. Couillet, J. Lega, E. Pampaloni, and C. Perez-Garcia, *Phys. Rev. Lett.* **65**, 2370 (1990).
[18] H. Tanaka and T. Araki, *Phys. Rev. Lett.* **81**, 389 (1998).
[19] Y. Shiwa, *Phys. Lett. A* **228**, 279 (1997).
[20] K.R. Elder, J. Viñals, and M. Grant, *Phys. Rev. Lett.* **68**, 3024 (1992); *Phys. Rev. A* **46**, 7618 (1992); M.C. Cross and D.I. Meiron, *Phys. Rev. Lett.* **75**, 2152 (1995); Q. Hou, S. Sasa, and N. Goldenfeld, *Physica A* **239**, 219 (1997); D. Boyer and J. Viñals, *Phys. Rev. E* **64**, 050101(R) (2001); see also L. Purvis

- and M. Dennin, Phys. Rev. Lett. **86**, 5898 (2001) on experimental measurements on domain coarsening in electroconvection.
- [21] M.C. Cross and P.C. Hohenberg, Rev. Mod. Phys. **65**, 851 (1993).
- [22] M.C. Cross, D. Meiron, and Yuhai Tu, Chaos **4**, 607 (1994).
- [23] C. Kittel, *Introduction to Solid State Physics* (Wiley, New York, 1986).
- [24] J. Swift and P.C. Hohenberg, Phys. Rev. A **15**, 319 (1977); P.C. Hohenberg and J. Swift, *ibid.* **46**, 4773 (1992).